

# Room-Temperature Magnetic Skyrmions in Pt/Co/Cu Multilayers

Shuyu Cheng,<sup>1</sup> Núria Bagués,<sup>2</sup> Camelia M. Selcu,<sup>1,\*</sup> Jacob B. Freyermuth,<sup>1</sup> Ziling Li,<sup>1</sup> Binbin Wang,<sup>2</sup> Shekhar Das,<sup>1</sup> P. Chris Hammel,<sup>1</sup> Mohit Randeria,<sup>1</sup> David W. McComb,<sup>2,†</sup> and Roland K. Kawakami<sup>1,‡</sup>

<sup>1</sup>*Department of Physics, The Ohio State University, Columbus, Ohio 43210, United States*

<sup>2</sup>*Department of Materials Science and Engineering,  
The Ohio State University, Columbus, Ohio 43210, United States*

Magnetic skyrmions are promising for next-generation information storage and processing owing to their potential advantages in data storage density, robustness, and energy efficiency. The magnetic multilayers consisting of Pt, Co, and a third metal element  $X$  provide an ideal platform to study the skyrmions due to their highly tunable magnetic properties. Here, we report the observation of room-temperature bubble-like Néel skyrmions in epitaxial Pt/Co/Cu multilayers in samples with multidomain states in zero field. The magneto-optic Kerr effect (MOKE) and superconducting quantum interference device (SQUID) magnetometry are applied to investigate the shapes of the hysteresis loops, the magnetic anisotropy, and the saturation magnetization. By tuning the Co thickness and the number of periods, we achieve perpendicular and in-plane magnetized states and multidomain states that are identified by a wasp-waisted hysteresis loop. Skyrmions are directly imaged by magnetic force microscopy (MFM) and Lorentz transmission electron microscopy (LTEM). The development of room-temperature skyrmions in Pt/Co/Cu multilayers may lead to advances in skyrmion-related research and applications.

Magnetic skyrmions are topologically protected spin textures that stand out as one of the strongest candidates for next-generation information storage due to their small sizes, thermal stability, and high energy efficiency [1–4]. These special spin textures originate from the complex interplay between exchange stiffness, magnetic anisotropy, dipolar interactions, applied field, and the Dzyaloshinskii-Moriya interaction (DMI). The DMI plays an important role in the stabilization of skyrmions, as it favors perpendicular alignment between neighboring spins [5, 6]. From a material point of view, the DMI is allowed by asymmetric crystal structures, which happens in bulk crystals that are non-centrosymmetric and at interfaces due to the broken mirror plane symmetry [7]. While the former gives rise to Bloch skyrmions in which the spins twist in the tangential direction [8, 9], the latter gives rise to Néel skyrmions in which the spins tumble in the radial direction [10, 11]. Though less common, Néel skyrmions could also form in bulk crystals when a mirror plane symmetry is broken [12].

Since 2009, magnetic skyrmions have been discovered in a variety of materials, including B20-phase materials [8, 9, 13], two-dimensional materials [14, 15], and magnetic bilayers and multilayers [10, 11, 16, 17]. Among these materials, the Pt/Co/ $X$  ( $X$  = metallic material) magnetic multilayers have drawn much attention because the insertion of the  $X$  layers into Pt/Co superlattices generates non-canceling interfacial DMI by breaking the inversion symmetry [10, 18, 19]. Furthermore, the magnetic properties of Pt/Co/ $X$  multilayers can be vastly tuned through varying the thickness of each layer [20, 21] and the number of repetitions of Pt/Co/ $X$  [22, 23], or

simply changing the element  $X$  [24, 25]. So far, the magnetic properties of Pt/Co/ $X$  multilayer systems with various metallic materials  $X$  has been reported including  $X$  = Mn [26], Ni [27], Cu [20], Ru [28], Ho [29], Ta [11], W [22], Ir [10], etc. Within a number of options for transition metal  $X$ , Cu is of particular interest for a number of reasons. Since the lattice constant of Cu is close to that of Co and Pt, it is possible to grow Pt/Co/Cu multilayers epitaxially along the Pt(111) direction [20]. This enables the layer-by-layer growth of high-quality crystalline Pt/Co/Cu multilayers using molecular beam epitaxy (MBE). Previous studies also reported that the Pt/Co/Cu multilayers have no magnetic dead layer as compared to other materials as  $X$  layer [24]. For these reasons, Pt/Co/Cu could be a model system to investigate skyrmion properties.

In this paper, we report the observation of room-temperature bubble-like Néel skyrmions in epitaxial Pt/Co/Cu multilayers, which was achieved by applying an out-of-plane (OOP) magnetic field to samples with a zero-field multidomain state. We used magneto-optic Kerr effect (MOKE) and magnetic force microscopy (MFM) to investigate how the zero-field magnetic states depend on the Co thickness ( $t_{Co}$ ) and number of periods  $N$ . We observed a spin-reorientation transition from OOP-magnetized to multidomain to in-plane (IP) magnetized with increasing  $t_{Co}$ , and a transition from OOP-magnetized to multidomain with increasing  $N$ . The multidomain states of interest could be recognized by the wasp-waisted shapes their OOP MOKE loops, and applying an OOP field generated skyrmions as observed by Lorentz transmission electron microscopy (LTEM) and MFM. In addition, since we developed the growth of epitaxial [Pt/Co/Cu] $_N$  multilayers on an insulating substrate, we were able to apply current pulses which assisted in the nucleation of skyrmions. To better understand the properties of the skyrmions and the mul-

\* selcu.1@osu.edu

† mccomb.29@osu.edu

‡ kawakami.15@osu.edu

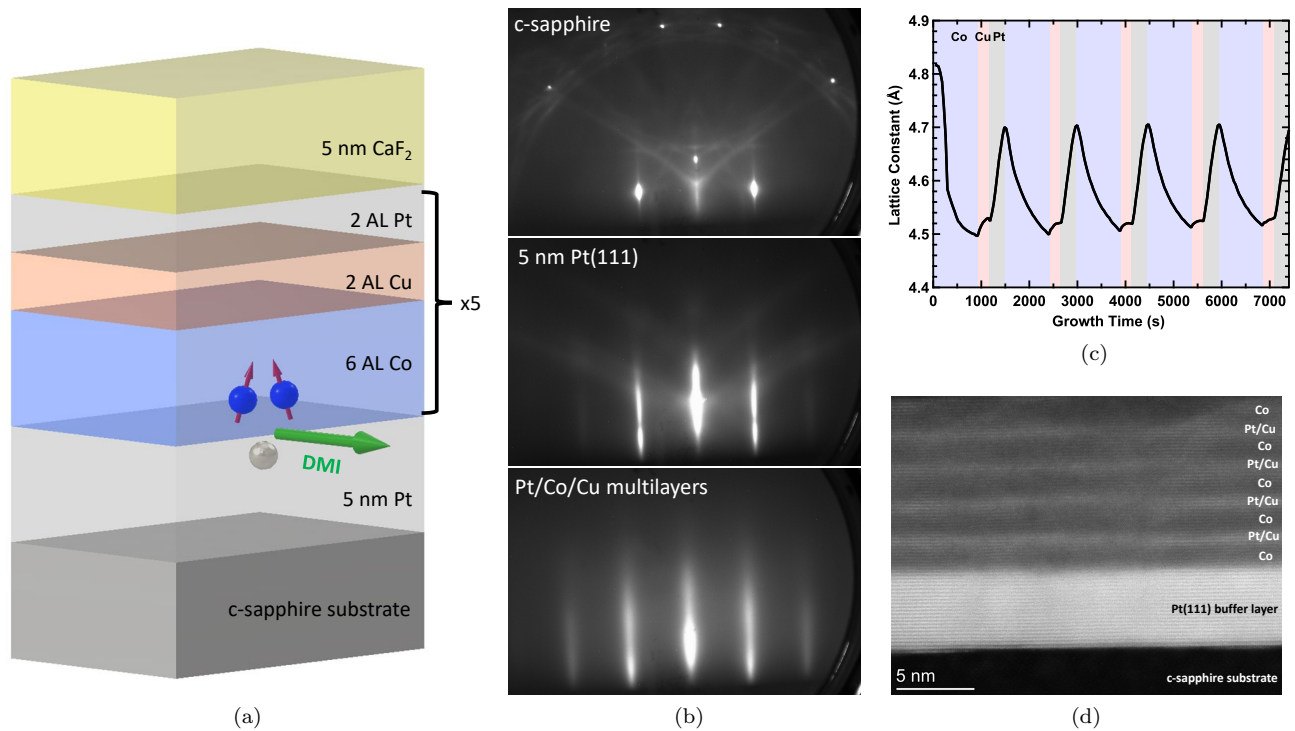


FIG. 1. Material growth and structural characterization. (a) Schematic drawing of the sample structure. (b) *In situ* RHEED patterns during growth. Top: sapphire(0001) with the beam along the  $[11\bar{2}0]$  in-plane direction. Middle: Pt(111). Bottom:  $[\text{Pt}(2)/\text{Co}(6)/\text{Cu}(2)]_5$  multilayers. (c) In-plane lattice constant extracted from the RHEED streak spacing during the growth. The blue, red, and gray regions correspond to the deposition of Co, Cu, and Pt, respectively. (d) STEM-HAADF image of  $[\text{Pt}(2)/\text{Co}(6)/\text{Cu}(2)]_5$  multilayers.

tidomain states, we employed micromagnetic simulations which were able to reproduce the skyrmion size, the domain size in the multidomain state, and the transition from OOP-magnetized to multidomain with increasing  $N$ .

The  $[\text{Pt}/\text{Co}/\text{Cu}]_N$  multilayers were grown on epitaxial Pt(111) buffer layers on  $\text{Al}_2\text{O}_3(0001)$  substrates (MTI Corporation) using MBE. Unless otherwise noted, the structure of the multilayer samples is (bottom to top): 5 nm Pt/[6 atomic layers (6 AL) Co/2 AL Cu/2 AL Pt] $_5$ /5 nm  $\text{CaF}_2$  (hereafter  $[\text{Pt}(2)/\text{Co}(6)/\text{Cu}(2)]_5$ , where the sequence of the layers is from the bottom to the top, and the numbers in the parentheses represent the thickness of each layer in units of atomic layers), as shown in Figure 1a. Prior to the growth, the  $\text{Al}_2\text{O}_3(0001)$  substrates were annealed in air at 1000 °C for 180 minutes and then degassed in the growth chamber at 500 °C for 30 minutes. A 5 nm Pt(111) buffer layer was epitaxially grown on the  $\text{Al}_2\text{O}_3(0001)$  substrate following the recipe described in [30].  $[\text{Pt}/\text{Co}/\text{Cu}]_N$  multilayers were deposited on top of the Pt(111) buffer layer at room temperature (RT) by opening and closing the shutters sequentially. The growth time for each layer was determined by the growth rate which was calibrated by a quartz crystal deposition monitor. Pt was deposited from an electron-beam evaporator, while Co and Cu were de-

posited from Knudsen cells. The typical growth rates for Pt, Co, and Cu are 0.9 Å/min, 0.8 Å/min, and 1.0 Å/min, respectively. After growth, 5 nm  $\text{CaF}_2$  was deposited on the sample to protect the sample from oxidation. The *in situ* reflection high-energy electron diffraction (RHEED) pattern was monitored during the growth, as shown in Figure 1b. Streaky RHEED patterns indicate that the  $[\text{Pt}(2)/\text{Co}(6)/\text{Cu}(2)]_5$  multilayers grow epitaxially. Furthermore, the in-plane lattice constant extracted from the RHEED pattern during growth shows oscillatory behavior, with decreasing lattice constant during Co layer growth, and increasing lattice constant during Cu and Pt layer growth, as shown in Figure 1c. This oscillation of in-plane lattice constant does not decay during the growth.

The structure of the sample was confirmed by scanning transmission electron microscopy (STEM) imaging of a cross-section sample using a ThermoFisher probe corrected Themis-Z at 300 kV. The cross-section sample was prepared by Ga ion milling at 30 kV and 5 kV using a focused ion beam (FIB). Figure 1d shows a STEM high-angle annular dark field (HAADF) image of  $[\text{Pt}(2)/\text{Co}(6)/\text{Cu}(2)]_5$  multilayer on top of Pt buffer layer on  $\text{Al}_2\text{O}_3$  viewed along the  $\text{Al}_2\text{O}_3$ - $[\bar{1}100]$  axis. In Figure 1d, the  $[\text{Pt}(2)/\text{Co}(6)/\text{Cu}(2)]_5$  sample exhibits well-defined layered structures. Due to atomic number

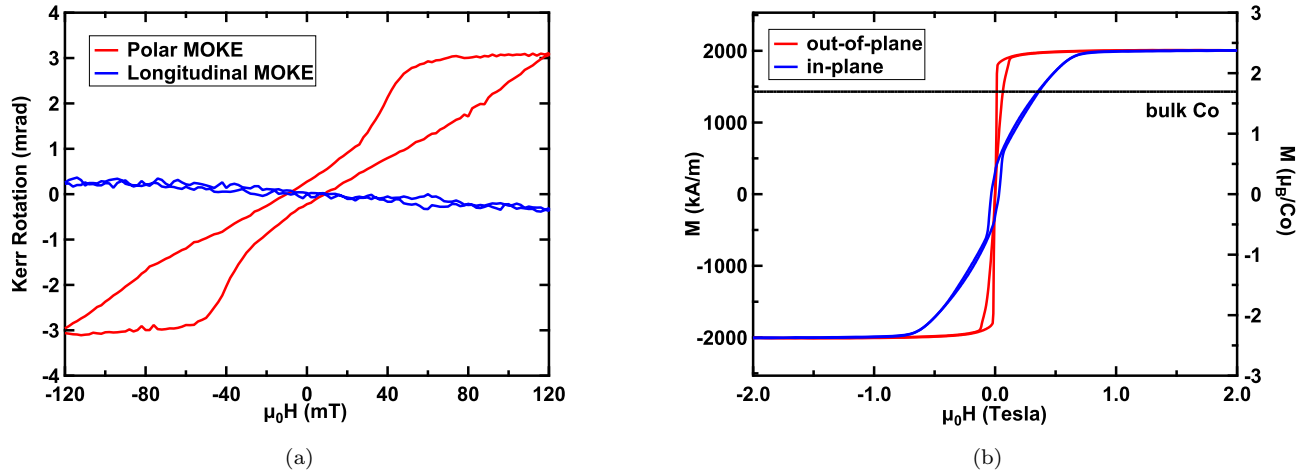


FIG. 2. Magnetic characterizations of  $[\text{Pt}(2)/\text{Co}(6)/\text{Cu}(2)]_5$  multilayers. (a) MOKE hysteresis loops of  $[\text{Pt}(2)/\text{Co}(6)/\text{Cu}(2)]_5$  multilayers. (b) SQUID hysteresis loops of  $[\text{Pt}(2)/\text{Co}(6)/\text{Cu}(2)]_5$  multilayers. The black solid line represents 1430 kA/m, which is the saturation magnetization of bulk Co.

(Z-) contrast in HAADF images the Co layers appear as dark layers in the STEM image, while the Pt and Cu layers appear as bright layers.

We first discuss MOKE and SQUID measurements of  $[\text{Pt}(2)/\text{Co}(6)/\text{Cu}(2)]_5$  multilayers. The MOKE measurement utilized a 632.8 nm laser and employed normal incidence for polar loops and a  $45^\circ$  angle of incidence for longitudinal loops. Figure 2a shows the polar (red curve) and longitudinal (blue curve) MOKE hysteresis loops of a  $[\text{Pt}(2)/\text{Co}(6)/\text{Cu}(2)]_5$  multilayer. The polar MOKE hysteresis loop shows a “wasp-waisted” shape with small remanence. Although the applied magnetic field was limited to 120 mT which is not sufficient to fully saturate the sample, the hysteresis loop nevertheless captures the main magnetic characteristics of the sample. Fully saturated loops were measured by SQUID (Figure 2b) and are discussed below. The wasp-waisted shape of the hysteresis loop is similar to that of Pt/Co/Cu multilayers near the spin-reorientation transition (SRT), where magnetic stripe domains with OOP easy axis were observed [20]. Meanwhile, the longitudinal MOKE hysteresis loop shows almost linear behavior in 120 mT range, with a much smaller magnitude compared to polar MOKE. The response to external magnetic fields where the magnetization is easier to polarize out-of-plane compared to in-plane is due to the presence of perpendicular surface magnetic anisotropy from the Pt/Co interfaces.

The results from SQUID measurements of  $[\text{Pt}(2)/\text{Co}(6)/\text{Cu}(2)]_5$  are shown in Figure 2b. The out-of-plane hysteresis loop (red curve) shows a similar shape to the polar MOKE loop, with low remanence and a saturation field of 192 mT, while the in-plane hysteresis loop (blue curve) saturates at  $\sim 0.7$  Tesla. We note that the saturation magnetization of  $[\text{Pt}(2)/\text{Co}(6)/\text{Cu}(2)]_5$  multilayers is measured to be  $2010 \pm 200$  kA/m, where

the uncertainty is mainly from the uncertainty in film thickness ( $\sim 10\%$ ). This is larger than the bulk Co value (1430 kA/m) [31] by the amount of  $\Delta M_{\text{Co}} = 580 \pm 200$  kA/m. The additional magnetic moment comes from Pt and is induced by the magnetic proximity effect, which has been reported in Pt/Co multilayers [32]. To quantify this effect, we calculate the magnetic moment of Pt from the following formula [32]:

$$\Delta M_{\text{Co}} t_{\text{Co}}^{\text{total}} = M_{\text{Pt}} t_{\text{Pt}}^{\text{total}} \quad (1)$$

Since most of the Pt moment concentrate in the first two atomic layers of Pt adjacent to the Co layers [33], here we take the thickness of 10 atomic layers of Pt, i.e. 2.3 nm, as  $t_{\text{Pt}}^{\text{total}}$ . By substituting  $t_{\text{Co}}^{\text{total}} = 6.1 \pm 0.6$  nm and  $t_{\text{Pt}}^{\text{total}} = 2.3 \pm 0.2$  nm into Eq. 1, we get  $M_{\text{Pt}} = 2.6 \pm 0.7 \mu_B/\text{Pt}$ .

For tuning the hysteresis loop shape and magnetic anisotropy, we varied the Co thickness and the number of periods  $N$ . For these studies, we maintained a constant thickness of 2 AL for the Pt and Cu layers.

Beginning with the Co thickness, we synthesized a sample series of with  $t_{\text{Co}} = 4, 5, 6, 7, 8$  and 9 AL for a fixed number of periods  $N = 5$ . Representative polar (red curve) and longitudinal (blue curve) MOKE loops are shown in Figure 3a. At a low Co thickness of 4 AL (sample I), the polar loop is square with a large remanence while the longitudinal loop has a small signal with no remanence. This indicates a perpendicular (out-of-plane) magnetic easy axis. As  $t_{\text{Co}}$  increases, the polar MOKE hysteresis loop evolves to a wasp-waist shape with low remanence for  $t_{\text{Co}} = 6$  AL (sample III), and eventually to almost linear with negligible hysteresis and zero remanences for  $t_{\text{Co}} = 8$  AL. Meanwhile, the longitudinal MOKE hysteresis loop exhibits an increasing remanence with thickness, going from zero remanences for  $t_{\text{Co}} = 4$  and 6 AL to a loop with substantial remanence and sharp

Sample ID	Co thickness $t_{Co}$	Number of periods $N$	Zero-field magnetic state
I	4	5	OOP
II	5	5	OOP
III	6	5	Multidomain
IV	7	3	OOP
V	7	4	OOP
VI	7	5	Multidomain
VII	7	7	Multidomain
VIII	8	4	Multidomain
IX	8	5	IP
X	9	5	IP

TABLE I. Summary of the structures and zero-field magnetic states of the samples.

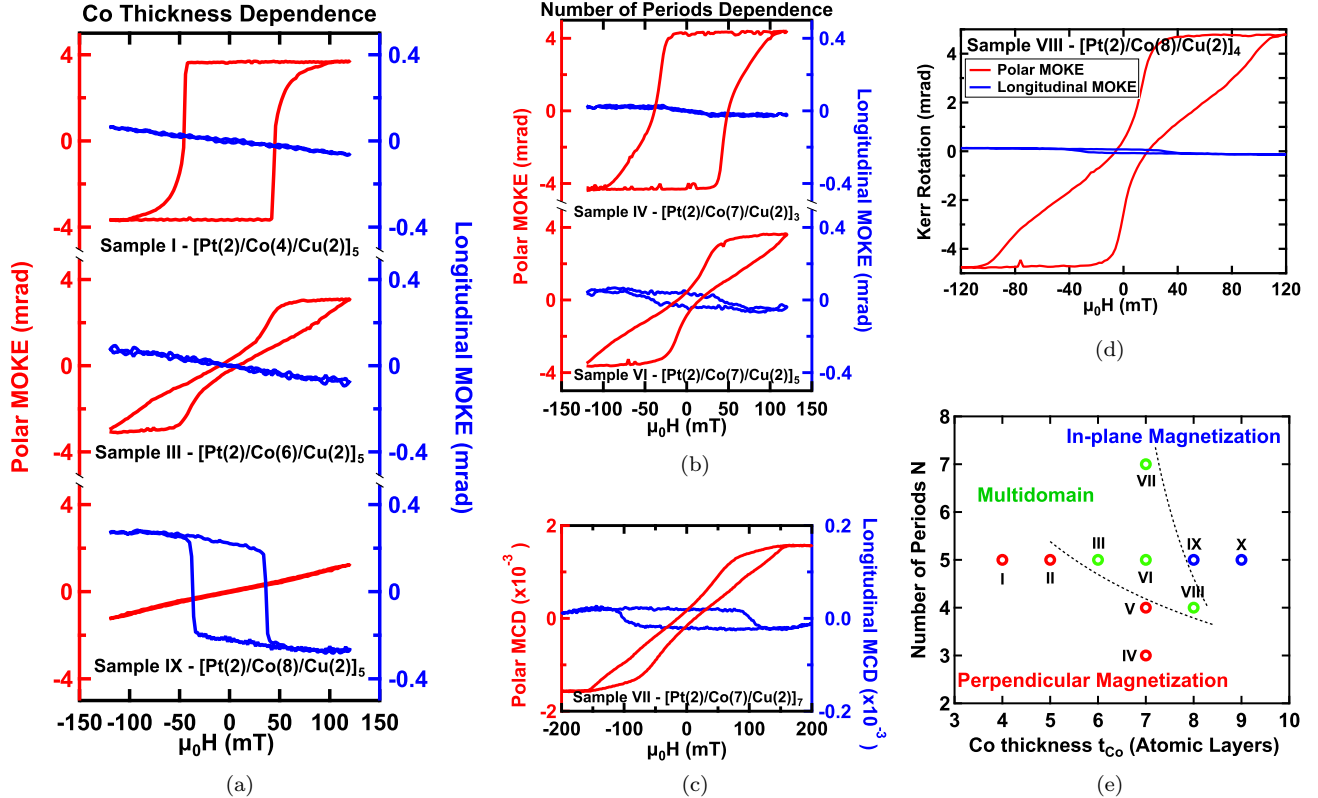


FIG. 3. Relationship between MOKE hysteresis loops and the multilayer structure. (a) Representative polar (red curve) and longitudinal (blue curve) MOKE hysteresis loops of  $[\text{Pt}(2)/\text{Co}(t_{Co})/\text{Cu}(2)]_5$  multilayers with a fixed number of periods  $N = 5$ . (b) Representative polar (red curve) and longitudinal (blue curve) MOKE hysteresis loops of  $[\text{Pt}(2)/\text{Co}(7)/\text{Cu}(2)]_N$  multilayers with fixed Co layer thickness  $t_{Co} = 7$  AL. (c) Polar (red curve) and longitudinal (blue curve) MCD hysteresis loops of  $[\text{Pt}(2)/\text{Co}(7)/\text{Cu}(2)]_7$  (sample VII) acquired on another setup.

(d) Polar (red curve) and longitudinal (blue curve) MOKE hysteresis loops of  $[\text{Pt}(2)/\text{Co}(8)/\text{Cu}(2)]_4$  (sample VIII). (e) Summary of the sample series. The dashed lines are guides to the eye.

magnetization reversals for 8 AL. This indicates a transition to in-plane magnetization for thicker Co. This spin reorientation transition from perpendicular magnetization to in-plane magnetization with increasing Co thickness is summarized by the horizontal points at  $N = 5$  in Figure 3e, with red points signifying perpendicular magnetization, green points signifying the multidomain SRT region (the domain structure has been verified by MFM and LTEM elsewhere in this manuscript), and blue points

signifying in-plane magnetization.

This thickness-dependent spin reorientation is understood as a competition between the perpendicular magnetic anisotropy (PMA) originating from the Pt/Co interface and the magnetic shape anisotropy favoring in-plane magnetization [34]. The Pt/Co PMA is interfacial so its energy density scales inversely with Co thickness. On the other hand, the shape anisotropy is bulk-like so its energy density remains constant as Co thickness is varied.

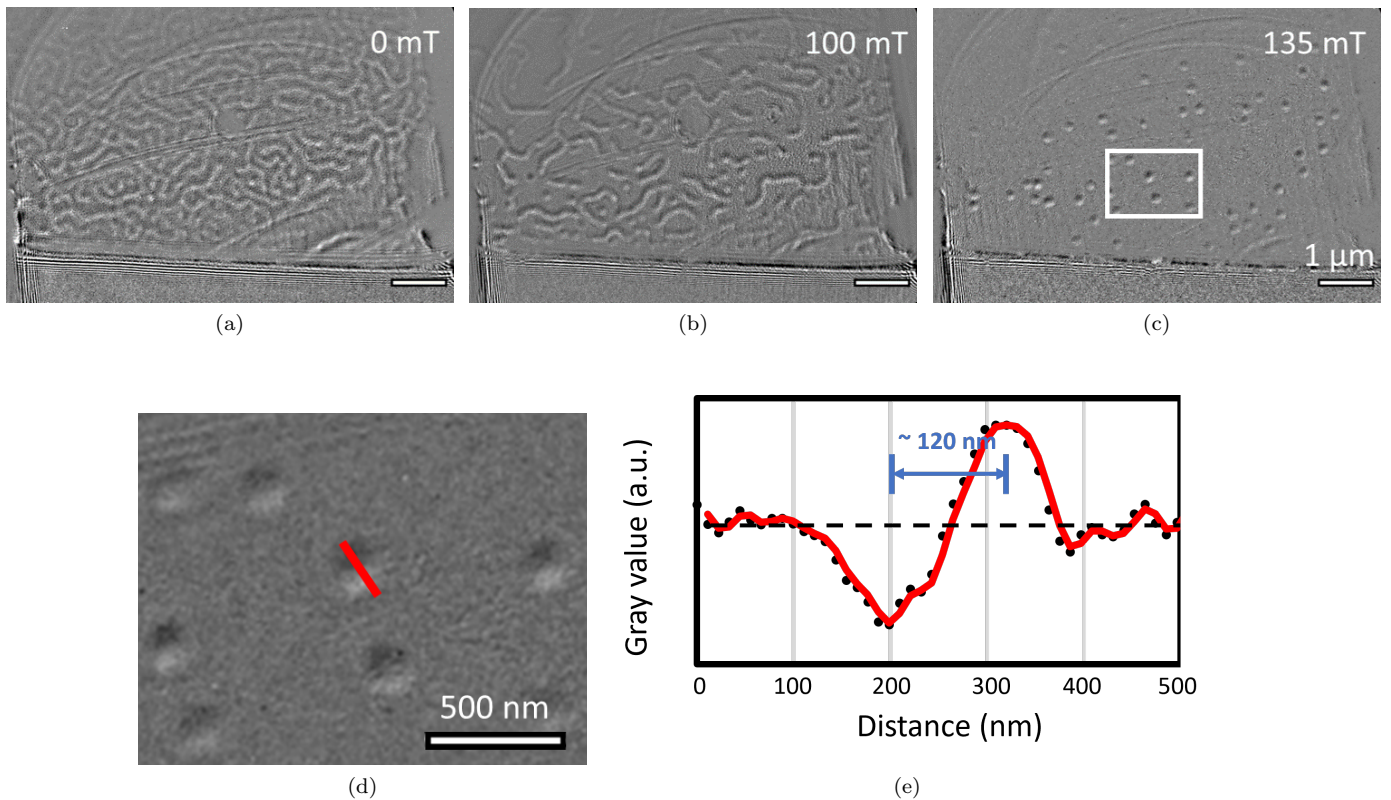


FIG. 4. LTEM images of the [Pt(2)/Co(6)/Cu(2)]<sub>5</sub> thin film with a thinned substrate. (a-c) LTEM images of the [Pt(2)/Co(6)/Cu(2)]<sub>5</sub> sample under (a) 0 mT, (b) 100 mT, and (c) 135 mT applied magnetic field. The scale bar represents 1 μm. (d). Zoomed-in LTEM image at 135 mT. The area of this image corresponds to the white box in Figure 4c. The scale bar represents 500 nm. (A background image taken in the field-polarized state (160 mT) is subtracted from (a - d) to improve the contrast. (e). Line-cut profile of a single skyrmion along the direction of the red line in Figure 4d. The red solid line is a smoothed curve of the line-cut profile.

Thus, larger thicknesses will favor in-plane magnetization while smaller thicknesses will favor perpendicular magnetization. We estimated the spin-reorientation thickness  $d_{Co}$  of individual Co layer by balancing the uniaxial anisotropy and magnetic dipolar energy (see SM section S2 for details). Taking magnetocrystalline anisotropy of hcp-structured cobalt  $K_{MC} = 0.43 \times 10^6 \text{ J/m}^3$  from [35], and interfacial anisotropy  $K_S = 0.9 \times 10^{-3} \text{ J/m}^2$  from the analysis of our SQUID data, the spin-reorientation thickness of cobalt is estimated to be 1.7 nm. This is in good agreement with our experimental results.

The hysteresis loops also exhibit variation as a function of the number of periods  $N$  of the Pt/Co/Cu multilayer. Figure 3b shows the out-of-plane and in-plane hysteresis loops for [Pt(2)/Co(7)/Cu(2)] <sub>$N$</sub>  for  $N = 3, 5,$  and  $7$ . In this sample series, sample IV with 3 periods has a polar MOKE loop (red curve, top loop) with nearly 100% remanence and a longitudinal MOKE loop (blue curve, top loop) with a weak response, indicating perpendicular magnetization. For sample VI with 5 periods, the polar MOKE loop (red curve, middle loop) has a wasp-waisted shape and the longitudinal MOKE loop shows a small signal with non-zero remanence. Similar to the

wasp-waisted polar loops of Figure 2a and sample III in Figure 3a, the loop is not fully saturated so these are minor loops. Nevertheless, the applied field goes sufficiently high to reveal the wasp-waisted loop corresponding to a multidomain state (see MFM in SM, Section S4). The easy axis is predominantly OOP, but the presence of hysteresis in the longitudinal loop (blue curve, middle loop) suggests the emergence of a small in-plane magnetization component.

For sample VII with 7 periods, we measured the hysteresis loops on a different magneto-optic setup with higher magnetic fields to saturate the magnetization fully. Here, we measured magnetic circular dichroism using a 532 nm laser at a 45° angle of incidence. As shown in the lower panel of Figure 3b, the polar MCD measurement (red curve) exhibits an elongated wasp-waisted loop that saturates at ~170 mT. The longitudinal MCD measurement (blue curve) shows the presence of an in-plane component of magnetization. These loops are characteristic of a multidomain state, which was directly confirmed by MFM (see SM, section S4). We note that the presence of multidomains for large  $N$  is consistent with prior MOKE microscopy measurements of Pt/Co/Cu samples



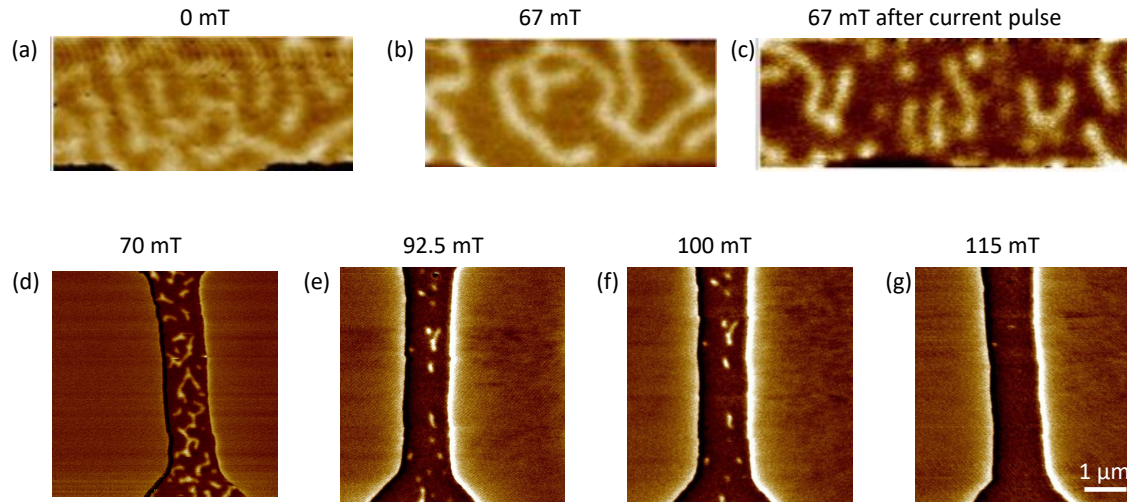


FIG. 5. MFM images of skyrmions. (a-c) For a  $[\text{Pt}(2)/\text{Co}(6)/\text{Cu}(2)]_5$  sample, the magnetic field is ramped from  $-100$  mT to  $0$  mT leading to labyrinth domains (a), ramping to  $67$  mT produces domains with lower density (b), and application of a current pulse generates isolated skyrmions (c). (d-f) For a  $[\text{Pt}(2)/\text{Co}(8)/\text{Cu}(2)]_4$  sample, the magnetic field is ramped from  $-100$  mT to  $70$  mT (d),  $92.5$  mT (e),  $100$  mT (f), and  $115$  mT (g). With increasing field, magnetic textures evolve from stripe domains to skyrmions to a field-polarized state.

with  $N = 10$  [20]. The transition from a perpendicularly magnetized state with high remanence at low  $N$ , to a multidomain structure with tilted hysteresis loops at higher  $N$  has been known for Pt/Co [36–38] and observed more recently in Pt/Co/X superlattices [39]. This transition is likely due to stronger dipolar fields, and hence stronger dipolar couplings that drive the stabilization of domains, as  $N$  increases. It is also worth noting that such dipolar fields could play an important role in stabilizing skyrmions [40, 41]. This transition was also reproduced by our micromagnetic simulations, as discussed later.

To further investigate the boundary of the multidomain region, we synthesized a sample with  $t_{\text{Co}} = 8$  AL and  $N = 4$  (sample VIII) that is to the lower-right of multidomain sample VI in the  $N - t_{\text{Co}}$  diagram (Fig. 3e). The polar and longitudinal MOKE loops for this sample (Figure 3d) confirm the wasp-waisted polar loop that is characteristic of a multidomain state.

The zero-field magnetic states of the samples are summarized in Table I and the hysteresis loops of each sample are shown in Section 1 of the Supplementary Material (SM).

We now focus on the samples in the transition region with wasp-waisted polar hysteresis loops, indicated by the green dots in Figure 3e (and labeled “Multidomain”). Here, we employed LTEM and MFM to image the magnetic domain structure and investigate the possible presence of skyrmions. For the LTEM measurements [42], focused ion beam (FIB) milling was utilized to thin the sapphire substrate, thus allowing the electron beam to transmit through the sample. Figure 4a-c shows planar-view LTEM images of a  $[\text{Pt}(2)/\text{Co}(6)/\text{Cu}(2)]_5$  multilayer sam-

ple at various out-of-plane magnetic fields. The straight parallel lines are from the substrate thinning and are not due to magnetic textures. For these images, we have tilted the sample by  $20^\circ$  to achieve magnetic contrast for Néel skyrmions [18, 43].

Beginning at zero field (Figure 4a), we observe labyrinth magnetic domains which evolve into magnetic stripe domains when the field is ramped up to  $100$  mT (Figure 4b). When the field is raised to  $135$  mT (Figure 4c), several magnetic bubbles are observed. The images in Figure 4(a - d) have improved contrast after subtracting a background image taken in the field-polarized state at  $160$  mT [44].

These bubbles are identified as Néel skyrmions based on the following considerations. First, there is no magnetic contrast when the electron beam is normally incident on the sample, which is the expected behavior since the Lorentz force is purely tangential for Néel skyrmions. Second, the magnetic contrast appears when the sample is tilted, and the bubble appears as having a positive and a negative lobe, which is the expected shape for Néel skyrmion [18]. Section S3 of the SM provides a detailed explanation of the LTEM contrast, which depends on the sample tilt and not the skyrmion chirality. A line-cut across the lobes, shown in Figure 4e (see SM section S3 for line-cut profiles at different fields), establishes the size of the bubble to be approximately  $120$  nm at  $135$  mT.

We further investigate the magnetic domain structure and skyrmion spin textures using MFM. An advantage of MFM over LTEM is that sample preparation including substrate thinning is not required. This provides access to the as-grown magnetic properties, as substrate

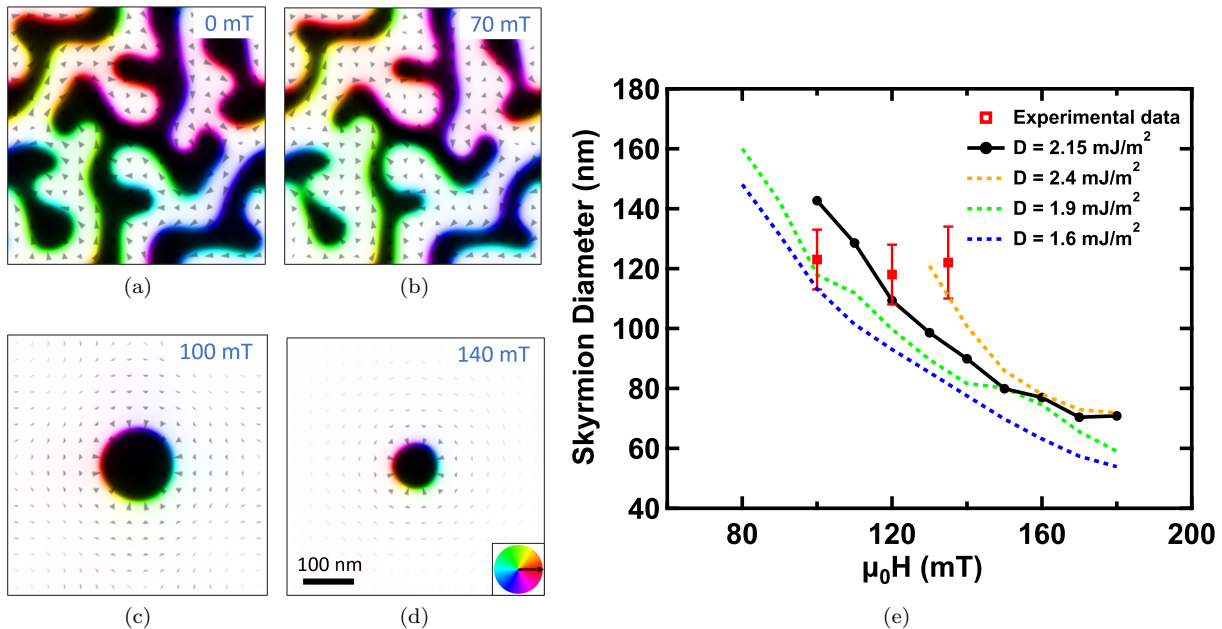


FIG. 6. (a-d) Micromagnetic simulation of  $[\text{Pt}(2)/\text{Co}(6)/\text{Cu}(2)]_5$  sample with (a) 0 mT, (b) 70 mT, (c) 100 mT (d) 140 mT applied field. The color wheel represents the in-plane component of the magnetization direction. (e). Simulated diameter of skyrmions as a function of applied field using several different DMI values. The red stars represent experimental data from LTEM measurements (see SM section S3 for line-cut profiles at different fields)

thinning could introduce strain. In addition, MFM measurements are compatible with devices fabricated by photolithography and electron-beam lithography. The measurements were performed in the Bruker MFM equipped with a homemade variable magnet with out-of-plane field range of -115 mT to 115 mT. The  $[\text{Pt}/\text{Co}/\text{Cu}]$  multilayers were patterned to have micron-wide device channels.

Upon investigating samples in the “Multidomain” region of the phase diagram (green dots in Figure 3e), we found that skyrmions could be nucleated either using field ramp sequences or current pulses. For a  $[\text{Pt}(2)/\text{Co}(6)/\text{Cu}(2)]_5$  sample (Figure 5a-c), the out-of-plane magnetic field was first set to -100 mT. Ramping to 0 mT produced labyrinth magnetic domains in the channel (Figure 5a). Fast Fourier transform (FFT) analysis of the MFM image yields an average labyrinth domain width of 130 nm at zero field. Increasing the field to 67 mT, the domain structure evolved to magnetic stripe domains with a lower density of domain walls (Figure 5b), consistent with the domain structures observed by LTEM (Figure 4b). As the MFM magnet is unable to reach the 135 mT needed to nucleate skyrmions, we decided to use current pulses to help nucleate skyrmions, as demonstrated previously in other materials [11, 45–47]. Following a single current pulse of  $1.39 \times 10^{12} \text{ A/m}^2$  with duration 20 ns, some of the stripe domains have broken up into isolated skyrmions (Figure 5c).

For a  $[\text{Pt}(2)/\text{Co}(8)/\text{Cu}(2)]_4$  sample, the saturation field is within the range of the MFM magnet, so we investigate skyrmion nucleation by field ramping. Starting by

applying a -100 mT field, we ramp up through 0 mT to a final field of 115 mT. Figure 5d-g show MFM images at representative fields. At 70 mT, the magnetic texture is dominated by stripe domains and a few skyrmions are observed. Increasing to 92.5 mT causes many of the stripes to nucleate into skyrmions or disappear altogether. At 100 mT, some of the skyrmions have disappeared, along with the stripes. Finally, at 115 mT, most of the sample has become field-polarized.

Additional MFM measurements establish the presence of skyrmions in a  $[\text{Pt}(2)/\text{Co}(7)/\text{Cu}(2)]_5$  sample (SM Section S4).

Micromagnetic simulations using MuMax3 [48] were performed to try to understand two important aspects of  $[\text{Pt}/\text{Co}/\text{Cu}]_N$  multilayers - out-of-plane ferromagnetic domain transition to multidomain transition, as well as the size of skyrmions. In our simulation, the  $[\text{Pt}(2)/\text{Co}(6)/\text{Cu}(2)]_N$  was modeled as a  $3N$ -layer stack, with the magnetic moment of the Co and Pt layers, the exchange coupling between the neighboring Co and Pt layers, and interlayer exchange coupling between neighboring Co layers taken into consideration. The interlayer exchange coupling between Co layers through Pt/Cu was set to be  $\sim 10\%$  of the exchange coupling within Co layers [33]. The micromagnetic parameters used were exchange stiffness  $A_{ex}$  of 25 pJ/m [49–51], uniaxial anisotropy  $K_u$  of  $1.2 \text{ MJ/m}^3$ , DMI strengths  $D$  of  $2.15 \text{ mJ/m}^2$  from [52], and saturation magnetization  $M_S$  of  $1.4 \times 10^6 \text{ A/m}$  and  $1.7 \times 10^6 \text{ A/m}$  for Co and Pt layers, respectively. The selection of each micromagnetic param-

eter is justified in the SM section S5.

We first investigated the transition from uniformly magnetized states to multidomain states as the number of periods  $N$  increases. In these simulations, the initial state was magnetized along the out-of-plane direction, with 1% of spins randomized to avoid unstable equilibrium states. Then the system was allowed to relax from the initial state at zero field. For  $N = 1$  to 4, the magnetization remains uniformly magnetized at zero field, while for  $N = 5$ , the uniformly magnetized state breaks into labyrinth domains at zero field (see SM Section S5 for details). This is because as  $N$  increases, the dipolar interaction increases and overcomes the exchange interaction that favors a uniformly magnetized state [40, 41, 46]. FFT analysis yields a labyrinth domain width of 120 nm at zero fields, in good agreement with the MFM data.

Many different values of  $A_{ex}$  were found in the literature, ranging from 10 pJ/m to 35 pJ/m [49–51, 53–57]. To investigate the influence of  $A_{ex}$  on multidomain formation, we lowered  $A_{ex}$  from 25 pJ/m to 10 pJ/m, which is another widely used value [53]. With smaller exchange stiffness, all of [Pt(2)/Co(6)/Cu(2)] $_N$  multilayers relaxed into multidomain states, because such a small exchange stiffness is not sufficient to maintain a uniformly magnetized state (see SM section S5 for details). In addition, with  $A_{ex} = 10$  pJ/m, the simulated labyrinth domain width is 55 nm, much smaller than the experimentally observed value. Therefore, the agreement of simulation and experiment for 25 pJ/m but not for 10 pJ/m indicates the exchange stiffness of cobalt in our samples is close to 25 pJ/m.

We next studied the skyrmion size and its dependence on various parameters using the same micromagnetic model. In these simulations, the system relaxes from a Néel skyrmion with  $\sim 75$  nm diameter. Results of the simulations for the [Pt(2)/Co(6)/Cu(2)] $_5$  sample are shown in Fig. 6. At zero field, the simulations show a labyrinth domain structure, consistent with both the MFM and LTEM (Fig. 6a). As the magnetic field is increased, Néel skyrmions can be stabilized starting around 80-90 mT. Continuing to increase the field causes the skyrmions to shrink, as shown in Fig. 6c and 6d. Comparing with experimental values of skyrmion size that show little variation with field (red squares in Fig. 6e), the simulated skyrmion size exhibits a stronger variation with field than is consistent with the experimental uncertainties (see SM section S3 for details on the analysis). The reason for this discrepancy is unclear. Nevertheless, the experimental values of the skyrmion size near 120 nm suggest that the value of the DMI falls in between 1.9 mJ/m $^2$  and 2.4 mJ/m $^2$  (see Fig. 6e). Another trend observed in the simulation is an increase in the skyrmion size with increasing values of  $D$ . These simulated dependencies of skyrmion size on  $D$  and magnetic field are in agreement with previous analytical results in Wang *et al.* [58].

The variation of skyrmion size with  $D$  is understood as follows. Intuitively, a skyrmion can be thought as being composed of an inner “core” region with magne-

tization antiparallel to the applied field, and an intermediate “wall” region where the magnetization rotates until it becomes parallel to the applied field in the “outside” region. The Zeeman energy is most important in the core and outside regions, so increasing the field will shrink the core and increase the outside ferromagnetic region to lower the Zeeman energy, which leads to a smaller skyrmion. The DMI is most important of the wall region, so with a larger  $D$ , the skyrmion can lower its overall energy by increasing the width of the wall even though the Zeeman and anisotropy energies will increase. Thus, the skyrmion size will get larger with increasing  $D$ .

In conclusion, we observed room-temperature skyrmions in [Pt/Co/Cu] $_N$  multilayers. By varying the number of periods  $N$  and the Co thickness, we tuned the magnetic state from perpendicularly magnetized to multidomain (wasp-waisted loop shape) to in-plane magnetized. Magnetic imaging by LTEM and MFM on multidomain samples showed that the magnetic spin texture evolves from labyrinth domains at low perpendicular magnetic fields to isolated skyrmion spin textures at higher fields. By tilting the sample during LTEM, we verified that the skyrmions are Néel type. MFM measurements on patterned devices showed that current pulses could nucleate skyrmions at lower magnetic fields compared to only ramping magnetic fields. While our imaging studies focused on the multidomain samples, we do not exclude the possibility of skyrmions in the OOP- or IP-magnetized samples. This work establishes Pt/Co/Cu multilayers as a model system for investigating room-temperature skyrmions in ultrathin epitaxial materials.

## ACKNOWLEDGMENTS

We acknowledge stimulating discussions with Denis Pelekhov. This work was supported by the DARPA TEE program under Grant No. D18AP00008. Z.L. was supported by AFOSR/MURI project 2DMagic FA9550-19-1-0390 and US Department of Energy DE-SC0016379. This research was partially supported by the Center for Emergent Materials, an NSF MRSEC, under award number DMR-2011876. Electron microscopy was performed at the Center for Electron Microscopy and Analysis (CEMAS) at The Ohio State University.

## AUTHOR CONTRIBUTIONS

S.C. synthesized the materials and performed the RHEED, MOKE, and SQUID measurements. N.B. and B.W. performed the TEM and LTEM measurements. C.M.S., Z.L., and S.D. performed the MFM measurements. Z.L. performed MCD measurements. S.C., J.B.F., M.R. and R.K.K. performed micromagnetic simulations. R.K.K., D.W.M, M.R., and P.C.H. conceived



the study. All authors participated in data analysis and preparation of the manuscript.

- 
- [1] A. Fert, V. Cros, and J. Sampaio, Skyrmions on the track, *Nature Nanotechnology* **8**, 152 (2013).
- [2] W. Koshihara, Y. Kaneko, J. Iwasaki, M. Kawasaki, Y. Tokura, and N. Nagaosa, Memory functions of magnetic skyrmions, *Japanese Journal of Applied Physics* **54**, 053001 (2015).
- [3] G. Finocchio, F. Büttner, R. Tomasello, M. Carpentieri, and M. Kläui, Magnetic skyrmions: from fundamental to applications, *Journal of Physics D: Applied Physics* **49**, 423001 (2016).
- [4] C. Back, V. Cros, H. Ebert, K. Everschor-Sitte, A. Fert, M. Garst, T. Ma, S. Mankovsky, T. Monchesky, M. Mostovoy, N. Nagaosa, S. Parkin, C. Pfleiderer, N. Reyren, A. Rosch, Y. Taguchi, Y. Tokura, K. von Bergmann, and J. Zang, The 2020 skyrmionics roadmap, *Journal of Physics D: Applied Physics* **53**, 363001 (2020).
- [5] I. Dzyaloshinsky, A thermodynamic theory of “weak” ferromagnetism of antiferromagnetics, *Journal of Physics and Chemistry of Solids* **4**, 241 (1958).
- [6] T. Moriya, Anisotropic superexchange interaction and weak ferromagnetism, *Physical Review* **120**, 91 (1960).
- [7] R. Wiesendanger, Nanoscale magnetic skyrmions in metallic films and multilayers: a new twist for spintronics, *Nature Reviews Materials* **1**, 1 (2016).
- [8] S. Mühlbauer, B. Binz, F. Jonietz, C. Pfleiderer, A. Rosch, A. Neubauer, R. Georgii, and P. Böni, Skyrmion lattice in a chiral magnet, *Science* **323**, 915 (2009).
- [9] X. Yu, Y. Onose, N. Kanazawa, J. H. Park, J. Han, Y. Matsui, N. Nagaosa, and Y. Tokura, Real-space observation of a two-dimensional skyrmion crystal, *Nature* **465**, 901 (2010).
- [10] C. Moreau-Luchaire, C. Moutafis, N. Reyren, J. Sampaio, C. Vaz, N. Van Horne, K. Bouzehouane, K. Garcia, C. Deranlot, P. Warnicke, P. Wohlhüter, J.-M. George, M. Weigand, J. Raabe, V. Cros, and A. Fert, Additive interfacial chiral interaction in multilayers for stabilization of small individual skyrmions at room temperature, *Nature Nanotechnology* **11**, 444 (2016).
- [11] S. Woo, K. Litzius, B. Krüger, M.-Y. Im, L. Caretta, K. Richter, M. Mann, A. Krone, R. M. Reeve, M. Weigand, P. Agrawal, I. Lemesch, M.-A. Mawass, P. Fischer, K. Mathias, and G. S. D. Beach, Observation of room-temperature magnetic skyrmions and their current-driven dynamics in ultrathin metallic ferromagnets, *Nature Materials* **15**, 501 (2016).
- [12] I. Kézsmárki, S. Bordács, P. Milde, E. Neuber, L. Eng, J. White, H. M. Rønnow, C. Dewhurst, M. Mochizuki, K. Yanai, H. Nakamura, D. Ehlers, V. Tsurkan, and A. Loidl, Néel-type skyrmion lattice with confined orientation in the polar magnetic semiconductor GaV<sub>4</sub>S<sub>8</sub>, *Nature Materials* **14**, 1116 (2015).
- [13] X. Yu, N. Kanazawa, Y. Onose, K. Kimoto, W. Zhang, S. Ishiwata, Y. Matsui, and Y. Tokura, Near room-temperature formation of a skyrmion crystal in thin-films of the helimagnet FeGe, *Nature Materials* **10**, 106 (2011).
- [14] B. Ding, Z. Li, G. Xu, H. Li, Z. Hou, E. Liu, X. Xi, F. Xu, Y. Yao, and W. Wang, Observation of magnetic skyrmion bubbles in a van der Waals ferromagnet Fe<sub>3</sub>GeTe<sub>2</sub>, *Nano Letters* **20**, 868 (2019).
- [15] Y. Wu, S. Zhang, J. Zhang, W. Wang, Y. L. Zhu, J. Hu, G. Yin, K. Wong, C. Fang, C. Wan, X. Han, Q. Shao, T. Taniguchi, K. Watanabe, J. Zang, Z. Mao, X. Zhang, and K. L. Wang, Néel-type skyrmion in WTe<sub>2</sub>/Fe<sub>3</sub>GeTe<sub>2</sub> van der Waals heterostructure, *Nature Communications* **11**, 1 (2020).
- [16] N. Romming, A. Kubetzka, C. Hanneken, K. von Bergmann, and R. Wiesendanger, Field-dependent size and shape of single magnetic skyrmions, *Physical Review Letters* **114**, 177203 (2015).
- [17] W. Jiang, G. Chen, K. Liu, J. Zang, S. G. Te Velthuis, and A. Hoffmann, Skyrmions in magnetic multilayers, *Physics Reports* **704**, 1 (2017).
- [18] S. McVitie, S. Hughes, K. Fallon, S. McFadzean, D. McGrouther, M. Krajinak, W. Legrand, D. Maccariello, S. Collin, K. Garcia, N. Reyren, V. Cros, A. Fert, K. Zeissler, and C. H. Marrows, A transmission electron microscope study of Néel skyrmion magnetic textures in multilayer thin film systems with large interfacial chiral interaction, *Scientific Reports* **8**, 1 (2018).
- [19] S. Schlotter, P. Agrawal, and G. S. Beach, Temperature dependence of the Dzyaloshinskii-Moriya interaction in Pt/Co/Cu thin film heterostructures, *Applied Physics Letters* **113**, 092402 (2018).
- [20] L. Sun, J. Liang, X. Xiao, C. Zhou, G. Chen, Y. Huo, and Y. Wu, Magnetic stripe domains of [Pt/Co/Cu]<sub>10</sub> multilayer near spin reorientation transition, *AIP Advances* **6**, 056109 (2016).
- [21] S. Bandiera, R. Sousa, B. Rodmacq, L. Lechevallier, and B. Dieny, Effect of a Cu spacer between Co and Pt layers on the structural and magnetic properties in (Co/Cu/Pt)<sub>5</sub>/Pt type multilayers, *Journal of Physics D: Applied Physics* **46**, 485003 (2013).
- [22] I. Benguettat-El Mokhtari, A. Mourkas, P. Ntetsika, I. Panagiotopoulos, Y. Roussigné, S. Cherif, A. Stashkevich, F. Kail, L. Chahed, and M. Belmeguenai, Interfacial Dzyaloshinskii-Moriya interaction, interface-induced damping and perpendicular magnetic anisotropy in Pt/Co/W based multilayers, *Journal of Applied Physics* **126**, 133902 (2019).
- [23] S. K. Jena, R. Islam, E. Milińska, M. M. Jakubowski, R. Minikayev, S. Lewińska, A. Lynnyk, A. Pietruczik, P. Aleszkiewicz, C. Autieri, and A. Wawro, Interfacial Dzyaloshinskii-Moriya interaction in the epitaxial W/Co/Pt multilayers, *Nanoscale* **13**, 7685 (2021).
- [24] M. Belmeguenai, Y. Roussigne, S. M. Cherif, A. Stashkevich, T. Petrisor, M. Nasui, and M. Gabor, Influence of the capping layer material on the interfacial Dzyaloshinskii-Moriya interaction in Pt/Co/capping layer structures probed by brillouin light scattering, *Journal of Physics D: Applied Physics* **52**, 125002 (2019).
- [25] F. Ajejas, Y. Sassi, W. Legrand, S. Collin, A. Thiaville, J. P. Garcia, S. Pizzini, N. Reyren, V. Cros, and A. Fert, Element-selective modulation of interfacial Dzyaloshinskii-Moriya interaction in Pt[Co]Metal based multilayers, arXiv preprint arXiv:2109.00761 (2021).

- [26] M. Lonsky, M.-W. Yoo, Y.-S. Huang, J. Qian, J.-M. Zuo, and A. Hoffmann, Structural and magnetic properties of Pt/Co/Mn-based multilayers, *Physical Review Materials* **6**, 054413 (2022).
- [27] J.-C. Rojas-Sánchez, P. Laczkowski, J. Sampaio, S. Collin, K. Bouzehouane, N. Reyren, H. Jaffrès, A. Mougin, and J.-M. George, Perpendicular magnetization reversal in Pt/[Co/Ni]<sub>3</sub>/Al multilayers via the spin hall effect of Pt, *Applied Physics Letters* **108**, 082406 (2016).
- [28] S. Karayev, P. D. Murray, D. Khadka, T. Thapaliya, K. Liu, and S. Huang, Interlayer exchange coupling in Pt/Co/Ru and Pt/Co/Ir superlattices, *Physical Review Materials* **3**, 041401 (2019).
- [29] L. Liu, X. Zhao, W. Liu, Y. Song, X. Zhao, and Z. Zhang, Influence of rare earth metal ho on the interfacial Dzyaloshinskii-Moriya interaction and spin torque efficiency in Pt/Co/Ho multilayers, *Nanoscale* **12**, 12444 (2020).
- [30] S. Cheng, B. Wang, I. Lyalin, N. Bagués, A. J. Bishop, D. W. McComb, and R. K. Kawakami, Atomic layer epitaxy of kagome magnet Fe<sub>3</sub>Sn<sub>2</sub> and Sn-modulated heterostructures, *APL Materials* **10**, 061112 (2022).
- [31] I. M. Billas, A. Chatelain, and W. A. de Heer, Magnetism from the atom to the bulk in iron, cobalt, and nickel clusters, *Science* **265**, 1682 (1994).
- [32] M. Bersweiler, K. Dumesnil, D. Lacour, and M. Hehn, Impact of buffer layer and pt thickness on the interface structure and magnetic properties in (Co/Pt) multilayers, *Journal of Physics: Condensed Matter* **28**, 336005 (2016).
- [33] A. Mukhopadhyay, S. K. Vayalil, D. Graulich, I. Ahamed, S. Francoual, A. Kashyap, T. Kuschel, and P. A. Kumar, Asymmetric modification of the magnetic proximity effect in Pt/Co/Pt trilayers by the insertion of a Ta buffer layer, *Physical Review B* **102**, 144435 (2020).
- [34] W. Zeper, F. Greidanus, P. Carcia, and C. Fincher, Perpendicular magnetic anisotropy and magneto-optical kerr effect of vapor-deposited Co/Pt-layered structures, *Journal of Applied Physics* **65**, 4971 (1989).
- [35] J. Alameda, F. Carmona, F. Salas, L. Alvarez-Prado, R. Morales, and G. Pérez, Effects of the initial stages of film growth on the magnetic anisotropy of obliquely-deposited cobalt thin films, *Journal of magnetism and magnetic materials* **154**, 249 (1996).
- [36] Y. Ochiai, S. Hashimoto, and K. Aso, Co/Pt and Co/Pd ultrathin-multilayered films as new magneto-optical recording materials, *IEEE Transactions on Magnetics* **25**, 3755 (1989).
- [37] C. J. Lin, G. L. Gorman, C. H. Lee, R. F. C. Farrow, E. E. Marinero, H. V. Do, H. Notarys, and C. J. Chien, Magnetic and structural properties of Co/Pt multilayers, *Journal of Magnetism and Magnetic Materials* **93**, 194 (1991).
- [38] X. Wang, Y. Wei, K. He, Y. Liu, Y. Huang, Q. Liu, J. Wang, and G. Han, Effect of the repeat number and co layer thickness on the magnetization reversal process in [Pt/Co(x)]<sub>N</sub> multilayers, *Journal of Physics D: Applied Physics* **53**, 215001 (2020).
- [39] X. Wang, A. Cao, S. Li, J. Tang, A. Du, H. Cheng, Y. Sun, H. Du, X. Zhang, and W. Zhao, Manipulating density of magnetic skyrmions via multilayer repetition and thermal annealing, *Physical Review B* **104**, 064421 (2021).
- [40] O. Boulle, J. Vogel, H. Yang, S. Pizzini, D. de Souza Chaves, A. Locatelli, T. O. Mentes, A. Sala, L. D. Buda-Prejbeanu, O. Klein, M. Belmeguenai, Y. Roussigné, A. Stashkevich, S. M. Chérif, L. Aballe, M. Foerster, M. Chshiev, S. Auffret, I. M. Miron, and G. Gaudin, Room-temperature chiral magnetic skyrmions in ultrathin magnetic nanostructures, *Nature Nanotechnology* **11**, 449 (2016).
- [41] F. Büttner, I. Lemesch, and G. S. D. Beach, Theory of isolated magnetic skyrmions: From fundamentals to room temperature applications, *Scientific Reports* **8**, 4464 (2018).
- [42] B. Wang, P.-k. Wu, N. Bagués Salguero, Q. Zheng, J. Yan, M. Randeria, and D. W. McComb, Stimulated nucleation of skyrmions in a centrosymmetric magnet, *ACS Nano* **15**, 13495 (2021).
- [43] M. Benitez, A. Hrabec, A. Mihai, T. Moore, G. Burnell, D. McGrouther, C. Marrows, and S. McVitie, Magnetic microscopy and topological stability of homochiral néel domain walls in a Pt/Co/AlO<sub>x</sub> trilayer, *Nature Communications* **6**, 8957 (2015).
- [44] B. Wang, N. Bagués, T. Liu, R. K. Kawakami, and D. W. McComb, Extracting weak magnetic contrast from complex background contrast in plan-view fege thin films, *Ultramicroscopy* **232**, 113395 (2022).
- [45] W. Jiang, P. Upadhyaya, W. Zhang, G. Yu, M. B. Jungfleisch, F. Y. Fradin, J. E. Pearson, Y. Tserkovnyak, K. L. Wang, O. Heinonen, S. G. E. t. Velthuis, and A. Hoffmann, Blowing magnetic skyrmion bubbles, *Science* **349**, 283 (2015).
- [46] I. Lemesch, K. Litzius, M. Böttcher, P. Bassirian, N. Kerber, D. Heinze, J. Zázvorka, F. Büttner, L. Caretta, M. Mann, M. Weigand, S. Finizio, J. Raabe, M.-Y. Im, H. Stoll, G. Schütz, B. Dupé, M. Kläui, and G. S. D. Beach, Current-Induced Skyrmion Generation through Morphological Thermal Transitions in Chiral Ferromagnetic Heterostructures, *Advanced Materials* **30**, 1805461 (2018).
- [47] R. Juge, N. Sisodia, J. U. Larrañaga, Q. Zhang, V. T. Pham, K. G. Rana, B. Sarpi, N. Mille, S. Stanesco, R. Belkhou, M.-A. Mawass, N. Novakovic-Marinkovic, F. Kronast, M. Weigand, J. Gräfe, S. Wintz, S. Finizio, J. Raabe, L. Aballe, M. Foerster, M. Belmeguenai, L. D. Buda-Prejbeanu, J. Pelloux-Prayer, J. M. Shaw, H. T. Nembach, L. Ranno, G. Gaudin, and O. Boulle, Skyrmions in synthetic antiferromagnets and their nucleation via electrical current and ultra-fast laser illumination, *Nature Communications* **13**, 4807 (2022).
- [48] A. Vansteenkiste, J. Leliaert, M. Dvornik, M. Helsen, F. Garcia-Sanchez, and B. Van Waeyenberge, The design and verification of MuMax3, *AIP advances* **4**, 107133 (2014).
- [49] M. Grimsditch, E. E. Fullerton, and R. L. Stamps, Exchange and anisotropy effects on spin waves in epitaxial Co films, *Physical Review B* **56**, 2617 (1997).
- [50] H. F. Ding, A. K. Schmid, D. Li, K. Y. Guslienko, and S. D. Bader, Magnetic Bistability of Co Nanodots, *Physical Review Letters* **94**, 157202 (2005).
- [51] W. Legrand, Y. Sassi, F. Ajejas, S. Collin, L. Bocher, H. Jia, M. Hoffmann, B. Zimmermann, S. Blügel, N. Reyren, V. Cros, and A. Thiaville, Spatial extent of the Dzyaloshinskii-Moriya interaction at metallic interfaces, *Physical Review Materials* **6**, 024408 (2022).

- [52] H. Jia, B. Zimmermann, M. Hoffmann, M. Sallermann, G. Bihlmayer, and S. Blügel, Material systems for FM-/AFM-coupled skyrmions in Co/Pt-based multilayers, *Physical Review Materials* **4**, 094407 (2020).
- [53] Appendix, in *Simple Models of Magnetism*, edited by R. Skomski (Oxford University Press, 2008) p. 289–318.
- [54] H. F. Ding, W. Wulfhekel, and J. Kirschner, Ultra sharp domain walls in the closure domain pattern of Co(0001), *Europhysics Letters* **57**, 100 (2002), publisher: IOP Publishing.
- [55] S. Vernon, S. Lindsay, and M. Stearns, Brillouin scattering from thermal magnons in a thin Co film, *Physical Review B* **29**, 4439 (1984).
- [56] X. Liu, M. Steiner, R. Sooryakumar, G. Prinz, R. Farrow, and G. Harp, Exchange stiffness, magnetization, and spin waves in cubic and hexagonal phases of cobalt, *Physical Review B* **53**, 12166 (1996).
- [57] G. Shirane, V. Minkiewicz, and R. Nathans, Spin waves in 3 d metals, *Journal of Applied Physics* **39**, 383 (1968).
- [58] X. Wang, H. Yuan, and X. Wang, A theory on skyrmion size, *Communications Physics* **1**, 31 (2018).